6

Improper Ferroelectric Domain Walls

D. M. Evans[1], Ch. Cochard[2], R. G. P. McQuaid[2], A. Cano[3], J. M. Gregg[2], and D. Meier[1]

[1]*Department of Materials Science and Engineering, Norwegian University of Science and Technology (NTNU), Trondheim, Norway*
[2]*Centre for Nanostructured Media, School of Mathematics and Physics, Queen's University Belfast, Belfast, United Kingdom*
[3]*Institut Néel, CNRS & Univ. Grenoble Alpes, Grenoble, France*

Interfaces in oxide materials offer amazing opportunities for fundamental and applied research, giving a new dimension to functional properties, such as magnetism, multiferroicity, and superconductivity. Ferroelectric domain walls have recently emerged as an intriguing type of interface, where the distinct features of these walls introduce the important element of spatial mobility, allowing for the real-time adjustment of position, density, and orientation (see Chapters 11 to 13). This mobility adds an additional degree of flexibility that enables domain walls to take an active role in future devices and hold great potential as functional 2D systems for electronics (Catalan et al. 2012; Meier 2015; Bednyakov et al. 2018).

In this chapter, we will focus on the specific physical properties at domain walls in ferroelectric materials where the spontaneous electric polarization appears as a by-product of a structural or magnetic phase transition, and not as its primary order parameter. This is fundamentally different compared to the *proper* ferroelectrics discussed in previous chapters—e.g. $BaTiO_3$, $LiNbO_3$, and $Pb(Zr_xTi_{1-x})O_3$. The systems of interest to us are referred to as *improper* ferroelectrics (Levanyuk and Sannikov 1974) and display special properties that are remarkably different from *proper* ferroelectrics. In Section 6.1, we will begin with a short introduction to the fundamentals of improper ferroelectricity, followed by a discussion of emergent functional domain wall properties in different improper ferroelectric model systems. Section 6.2 covers the broad variety of electronic states and application opportunities associated with improper ferroelectric domain walls in hexagonal manganites. Section 6.3 addresses electronic transport and manipulation of domain walls in boracites, and in Section 6.4, we will present additional magnetoelectric coupling phenomena that arise when the interaction of magnetic spins and electric charges gives rise to improper ferroelectricity. A perspective regarding future research and application opportunities of improper ferroelectric domain walls is given in Section 6.5.

D. M. Evans, Ch. Cochard, R. G. P. McQuaid, A. Cano, J. M. Gregg, and D. Meier, *Improper Ferroelectric Domain Walls* In: *Domain Walls: From Fundamental Properties to Nanotechnology Concepts*. Edited by: Dennis Meier, Jan Seidel, Marty Gregg, and Ramamoorthy Ramesh, Oxford University Press (2020).
DOI: 10.1093/oso/9780198862499.003.0006

6.1 Basic Background

As in standard ferroelectric domain walls (see Chapter 1), the domain walls in improper ferroelectrics separate regions with different orientations of the corresponding order parameter, and they are spatially mobile and can be injected, positioned, and erased on demand. The important difference is that the primary order parameter of improper ferroelectrics is not the electric polarization, which simply appears as a symmetry-enforced "collateral" effect (Levanyuk and Sannikov 1974; Tolédano and Tolédano 1987; Strukov and Levanyuk 1998). A classic example of an improper ferroelectric material is gadolinium molybdate, $Gd_2(MoO_4)_3$ (Keve et al. 1971), where the structural instability of the paraelectric parent phase results in a doubling of the unit cell volume, which leads to the formation of a polar axis—which is then accompanied by a spontaneous polarization. An outstanding magnetic counterpart is $TbMnO_3$ (Kimura et al. 2003), where the instability is with respect to a spiral magnetic order that also exhibits a polar axis.

From the symmetry point of view, the primary order parameter of improper ferroelectrics always breaks more symmetries than the electric polarization P (otherwise the system is referred to as *pseudoproper* (Tolédano and Tolédano 1987; Strukov and Levanyuk 1998; Wadhawan 2000)). This means that P alone does not suffice to describe the maximal polar subgroup of the corresponding paraelectric parent phase, so that, in this sense, the corresponding transition can be regarded as a meta-ferroelectric transition. In fact, even if the system is uniaxial from the ferroelectric point of view and P points along one crystallographic direction only, improper ferroelectricity requires a primary order parameter q with two or more components. Thus, the reduced transformation properties of some nth product of q with $n \geq 2$, rather than q itself, matches those of P: $P \propto q^n$, from which the nontrivial coupling between these two quantities can be read. For example, in the important case of the hexagonal manganites discussed below, $q = (q_1, q_2)$ is associated with a particular translation symmetry breaking of the lattice for which $P_z \propto \left(q_1^3 - 3q_1q_2^2\right)$ (Artyukhin et al. 2013; Cano 2014). In the case of spiral magnets such as $TbMnO_3$ or $MnWO_4$, in contrast, $q = (q_1, q_2)$ is associated with the cycloidal arrangement of the Mn spins, and the above product involves the gradient also: $P_z \propto (q_1 \nabla_x q_2 - q_2 \nabla_x q_1)$ for an xz-cycloid, implying a coupling term similar to a Lifshitz invariant that arises from spin–orbit interactions (Tolédano 2009; Cano and Levanyuk 2010; Tolédano et al. 2010; Sando et al. 2013).

Since the primary order parameter of improper ferroelectrics is not the electric polarization, different—generally less stringent—boundary conditions apply regarding the elastic and mechanical compatibility of associated domain walls (Tagantsev et al. 2010). Thus, a wide variety of unconventional—and otherwise energetically very unfavorable—electronic domain wall configurations arise in the as-grown state. In particular, charged domain walls with positive or negative domain wall bound charges can readily form (see Chapter 3, Figure 3.2(c) for an illustration) (Meier et al. 2012). This is a crucial and important difference compared to proper ferroelectrics, where rather special preparation procedures, such as frustrated electrical poling (Sluka et al. 2013), electrical trailing fields (Crassous et al. 2015), and photo-excitation of mobile carriers (Bednyakov et al. 2015), are typically required to introduce such charged walls. In improper ferroelectrics, on the contrary, charged domain walls are naturally observed as reported for, e.g. $RMnO_3$

(R = Sc, Y, In, Dy to Lu) (Meier et al. 2012; Wu et al. 2012; Meier et al. 2017), $Cu_3B_7O_{13}Cl$ (McQuaid et al. 2017), $(Ca,Sr)_3Ti_2O_7$ (Oh et al. 2015), $Mn_{1-x}Co_xWO_4$ (Leo et al. 2015), and $TbMnO_3$ (Matsubara et al. 2015a).

Although improper ferroelectrics usually exhibit a smaller spontaneous polarization than proper ferroelectrics (e.g. $\approx 5.5\ \mu C/cm^2$ in $YMnO_3$ (Fujimura et al. 1996; Van Aken et al. 2004) and $\lesssim 0.1\ \mu C/cm^2$ in $TbMnO_3$ (Kimura et al. 2003) compared to $\approx 20\ \mu C/cm^2$ in $BaTiO_3$ (Lines and Glass 2001; Merz 1949)), the locally diverging electrostatic potentials at the charged walls still require screening and hence a spatial redistribution of mobile carriers. For example, for $YMnO_3$, considerable carrier densities ($= 2P/q$) on the order of up to $\sim 6 \times 10^{13}$ per cm^2 are expected to arise to screen the bound charges at 180° tail-to-tail walls (Meier et al. 2012). Because of this accumulation of mobile carriers, the domain wall conductivity at improper ferroelectric domain walls can be significantly higher than in the surrounding bulk as we explain in more detail in Sections 6.2 and 6.3. Thus, analogous to proper ferroelectric domain walls, improper ferroelectric domain walls develop unusual electronic properties, which makes them interesting as functional nanoscale entities for future electronics. Key advantages compared to conventional ferroelectrics are the abundance and stability of the charged domain walls, and the generally higher flexibility to host domain walls with different charge states, enabled by the subordinate nature of the induced ferroelectric order.

Several extended articles and review papers are now published that discuss the screening at charged domain walls (e.g. Eliseev et al. 2008; Catalan et al. 2012; Meier 2015; Bednyakov et al. 2018; Schoenherr et al. 2019), where the reader can find details about stability limits, screening mechanisms, and theoretical models. In the following, we will focus on instructive examples from the recent literature, highlighting the interesting physics and unique functionalities of improper ferroelectric domain walls based on selected materials.

6.2 Functional Domain Walls in Hexagonal Manganites

6.2.1 Domain Wall Structure

Probably the most intensively studied system with improper ferroelectric domain walls are the hexagonal manganites, $RMnO_3$ (R = Sc, Y, In, Dy to Lu). Hexagonal manganites exhibit ferroelectric order below a critical temperature $T_C \approx 1400$ K, with the polarization, P, pointing along the crystallographic c-axis (Van Aken et al. 2004; Lilienblum et al. 2015). Here, the primary symmetry-lowering order parameter is a unit-cell-tripling distortive mode, which breaks the $P6_3/mmc$ symmetry of the paraelectric phase and induces a structural non-centrosymmetric distortion (Fennie and Rabe 2005). This distortion leads to periodic tilts of the corner-shared MnO_5 bipyramids in $RMnO_3$ together with displacements of the R ions as illustrated in Figure 6.1(a), resulting in the characteristic displacement pattern seen in the high-angle annular dark field scanning transmission electron microscopy (HAADF-STEM); see Figure 6.1(b). As explained in Holtz et al. (2017), these displacements can be described by

$$u(r_n) = u_0 + Q_1 \cos q \cdot r_n + Q_2 \cos q \cdot r_n, \tag{6.1}$$

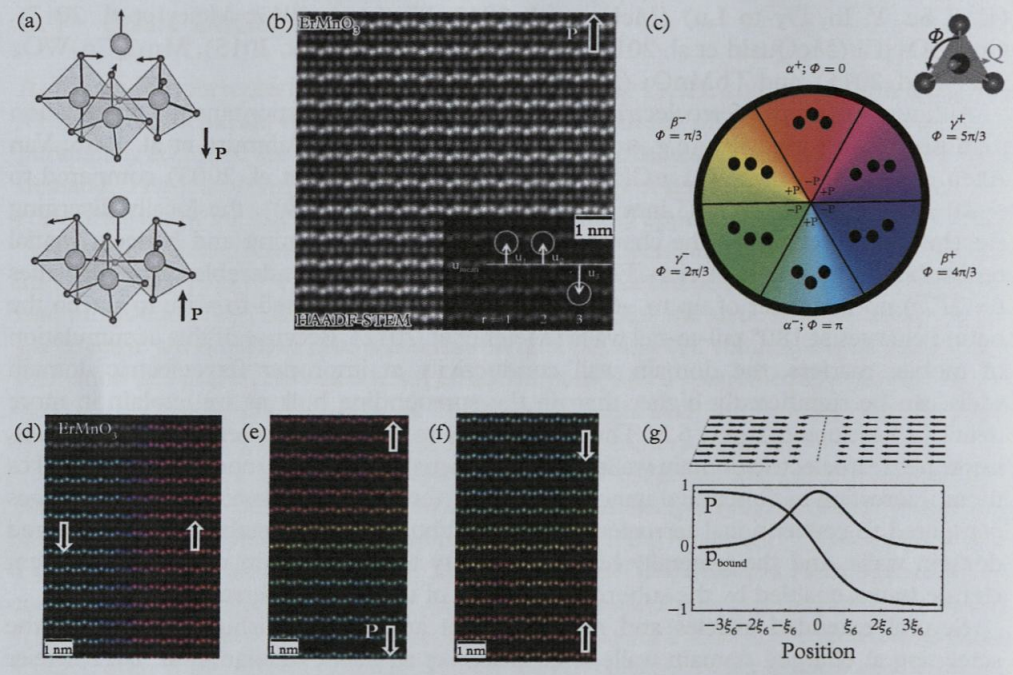

Figure 6.1 *Ferroelectric polarization and the domain walls in the hexagonal manganites. (a) Schematic showing the origin of the geometrically driven ferroelectric polarization: the tilt and deformation of MnO_5 bipyramids displaces the rare-earth ions leading to a spontaneous polarization along the [001] axis. (b) High-angle annular dark field scanning transmission electron microscopy (HAADF-STEM) of the $ErMnO_3$ viewed down the $[1\bar{1}0]$ zone axis; the bright atoms are Er, and the grey atoms are Mn: the former shows the characteristic corrugation that leads to ferroelectricity in these systems. (b) Schematic of the six possible domain configuration and colored to represent their differences with respect to the order parameter φ— see Equation (6.1). (d)–(f) HAADF-STEM of the three different domain wall orientations (neutral, tail-to-tail, and head-to-head), with the color overlay shown in (c) to illustrate the change in φ. (g) Trimerization at a head-to-head domain wall separating two regions of ferroic order. Note: Artyukhin et al. (2013) and Holtz et al. (2017) use φ or Φ, respectively, to describe the order parameter: there is no physical distinction, and it is only a question of terminology.*

Source: (a) Based on an original image from Fiebig et al. 2016. (b–g) are slightly adapted from Holtz et al. 2017, this is an unofficial adaptation of an article that appeared in an ACS publication. ACS has not endorsed the content of this adaptation or the context of its use.

where u_0 denotes a polar distortion ($\propto P$), while $Q_i\,(i = 1,2)$ represent the components of the primary structural order parameter $[Q = (Q_1, Q_2) = Q\cos\varphi, Q\sin\varphi]$ (Fennie and Rabe 2005; Artyukhin et al. 2013). Thus, $u(r_n)$ can be directly linked to the canonical Landau free energy of the system:

$$F(Q,T) = \frac{a(T)}{2}Q^2 + \frac{b}{4}Q^4 + \frac{1}{6}\left(c + c'\cos^2(3\varphi)\right)Q^6 + \frac{g}{2}\left[(\nabla Q)^2 + Q^2(\nabla\varphi)^2\right], \quad (6.2)$$

where the temperature dependence is given by the coefficient $a(T) = a'(T - T_C)$, with a', b, c, and g being positive constants (see Holtz et al. 2017 for details). Most importantly for the formation of domain walls in $R\mathrm{MnO_3}$, the anisotropy term in Equation (6.2) leads to six symmetry-equivalent domain states, i.e. six distinct displacement patterns as sketched in Figure 6.1(c), corresponding to values $\varphi_n = \frac{n\pi}{3}$ $(n = 0,\ldots,5)$. These six displacement patterns (up-up-down, up-down-up, etc.) represent the structural trimerization domains/anti-phase domains that form below T_C. The improper ferroelectric polarization then arises due to a coupling to Q, linked via the relation $P \sim Q^3 \cos 3\varphi$ as shown by Fennie and Rabe (2005), Artyukhin et al. (2013), and Cano (2014).

The structural trimerization domains are separated by comparatively narrow domain walls across which the trimerization phase changes from φ_n to φ_{n+1} over a distance of about 5 to 10 Å as shown in Figure 6.1(d–f) (Holtz et al. 2017). Along with Q, the direction of the electric polarization changes across the wall by 180°, going through zero at the center of the wall. The latter is shown for the case of a head-to-head domain wall in Figure 6.1(g). This figure further shows the density of bound charges that arises at such 180° domain walls, leading to a redistribution of mobile carriers that will be addressed in Section 6.2.2. Whenever trimerization domain walls intersect, they do so in characteristic sixfold meeting points. This results in structural vortices where the phase φ of the trimerization order parameter changes around the meeting points from 0 to 2π in a discrete fashion, which have attracted significant attention as a test system for cosmology-related questions (for details, we refer the interested reader to Griffin et al. 2012, Huang and Cheong 2017, and Meier et al. 2017). This special distribution of the trimerization order parameter is enabled by an intrinsically weak sixfold anisotropy (Artyukhin et al. 2013), which is further weakened by the coupling to the electric polarization (Cano 2014) and by driving the system near the transition owing to its universality class (Lilienblum et al. 2015). Since these vortices are topologically protected, the meeting points (i.e. the vortex cores) serve as anchor points for the domain walls in $R\mathrm{MnO_3}$, preventing the system from minimizing its energy by forming, e.g. simple stripe-like domains with neutral domain walls. This topology-driven effect explains why charged domain walls naturally occur in $R\mathrm{MnO_3}$ in the as-grown state. Figure 6.2(a) presents the resulting distribution of improper ferroelectric domains, with a multitude of sixfold meeting points and freely meandering domain walls in between them (Schaab et al. 2014) (note that with respect to the ferroelectric order, these meeting points represent so-called vertex structures). The image is obtained by piezoresponse force microscopy (PFM, in-plane contrast) where the bright and dark colors show ferroelectric domains with opposite polarization direction. Most importantly for the study of electronic domain wall states, due to the meandering wall structure seen in Figure 6.2(a), the local electrostatic configuration continuously varies between positively charged (head-to-head), neutral (side-by-side), and negatively charged (tail-to-tail) domain wall states, thus including all fundamental orientations of ferroelectric 180° walls (see Figure 6.1(d–f) high-resolution images). The manifestation of this broad variety of neutral and charged domain wall states in one material is a key property of the hexagonal manganites, turning the system

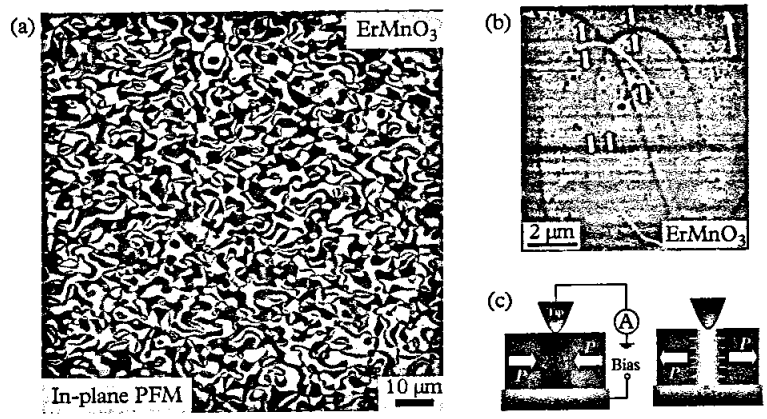

Figure 6.2 *Atomic force microscopy (AFM) images of domain and domain walls in the hexagonal manganites. (a) PFM image showing the ferroelectric domain structure with the iconic sixfold vertex meeting points. (b) Conductive atomic force microscopy (cAFM) image showing how conductivity depends on the domain walls' orientation relative to the unique polar axis: bright/dark areas show higher/lower conductivity compared to the bulk. (c) Schematic illustration of how the screening charges form at head-to-head and tail-to-tail domain walls. Simplistically, for p-type conductors, tail-to-tail walls have a build-up of majority carriers to screen the polar discontinuity, leading to an enhanced conductivity.*

Source: (a) Image slightly modified from original work by Schaab et al. (2014), with the permission of AIP Publishing. (b) and (c) are slightly modified from the original publication by Meier et al. (2012).

into an ideal playground for studying the physics at charged domain walls and the exploration of their functional properties.

6.2.2 Electronic Domain Wall Properties

The electronic transport at domain walls in hexagonal manganites is predominantly determined by the domain wall bound charges and the related electrostatic potential (Meier et al. 2012; Smaabraaten et al. 2018). This relation is also evident from the representative conductance map in Figure 6.2(b), which shows the local currents measured at the domain walls in hexagonal $ErMnO_3$. The data is recorded on the surface of a sample with in-plane-polarization ([1 1 0]-orientation) by conductive atomic force microscopy (cAFM), revealing tail-to-tail domain walls with enhanced conductance (bright) and head-to-head domain walls with suppressed conductance (dark) relative to the bulk. Between these two extreme cases, the domain wall conductance varies gradually, exhibiting bulk-like behavior at positions where the walls are oriented parallel to P and, hence, in a neutral configuration.

This emergence of anisotropic conductance at the domain walls and the general trend seen in the cAFM scan in Figure 6.2(b) can be understood based on the electronic bulk properties of $ErMnO_3$. The material is a p-type semiconductor with a small band gap of about 1.6 eV (Skjærvø et al. 2016; Schoenherr et al. 2019). The mobile majority carriers

(holes) within the material experience the pronounced electrostatic fields associated with the domain wall bound charges and redistribute accordingly, leading to hole accumulation at tail-to-tail walls and hole depletion at head-to-head walls as sketched in Figure 6.2(c). Typical current values that are measured at the conducting tail-to-tail walls in as-grown samples are on the order of 10 to 100 pA for bias voltages of about 3–5 V and sample thicknesses of ≈ 0.5 to 1 mm. First studies have demonstrated, however, that the domain wall currents can be manipulated, for example, by aliovalent doping (Hassanpour et al. 2016; Schaab et al. 2016; Holstad et al. 2018)—following established strategies known from semiconductor research—or by oxidizing/reducing the material, i.e. by changing the concentration of interstitial oxygen, which is responsible for the p-type characteristics in $R\mathrm{MnO_3}$ (Du et al. 2013; Skjærvø et al. 2016; Schaab et al. 2018). The latter reflects the general opportunity to control and optimize the electronic domain wall behavior, with the goal of achieving technologically relevant current densities in the nanoampere regime.

It is important to note, however, that a comprehensive characterization of the electronic transport at ferroelectric domain walls remains a challenging experimental task. While DC current measurements by cAFM provide valuable insight into relative changes in conductance with nanoscale spatial resolution, it is difficult to gain quantitative information from such scans. As cAFM is a two-probe measurement, it is crucial to carefully consider contributions from contact resistance and possible displacement currents. In addition, the typical width of ferroelectric domain walls ($\approx$10 Å) is well below the resolution of cAFM ($\gtrapprox$20 nm) and the spread of the injected currents, so that the detected signals necessarily represent a convolution of both sample- and probe-tip-related parameters that need to be carefully disentangled. More recently, microscopy approaches such as electrostatic force microscopy (EFM) (Schoenherr et al. 2019) and photoemission electron microscopy (PEEM) have been applied to study improper ferroelectric domain walls (Schaab et al. 2014; Pawlik et al. 2017). These microscopy measurements were successful in demonstrating that the anomalous electronic transport at the walls—previously measured by cAFM—is indeed an intrinsic phenomenon and not just an effect related to induced domain wall movements or extrinsic tip–sample interactions.

A first breakthrough toward a quantitative analysis of electronic domain wall properties has been the recent realization of local Hall measurements. Campbell et al. (2016) used patterned thin film contact pads, on the top surface of $\mathrm{YbMnO_3}$ single crystals, as source and drain electrodes to drive currents along conducting tail-to-tail domain walls. In the presence of an approximately perpendicular in-plane magnetic field, the scanned conducting tip in an AFM was used to monitor local surface potential changes that resulted from the Hall effect (Figure 6.3(a)). While the experiments were initially done using the AFM pick-up in contact mode (which required a separate calibration to obtain numerical values for Hall voltages), more refined subsequent experiments on $\mathrm{ErMnO_3}$ by Turner et al. (2018) used non-contact Kelvin probe force microscopy (KPFM) to directly and quantitatively determine the developed Hall voltages (Figure 6.3(b)).

These two Hall effect studies revealed several important aspects of the carrier behavior in tail-to-tail manganite domain walls: first, that the active carriers are p-type, as expected;

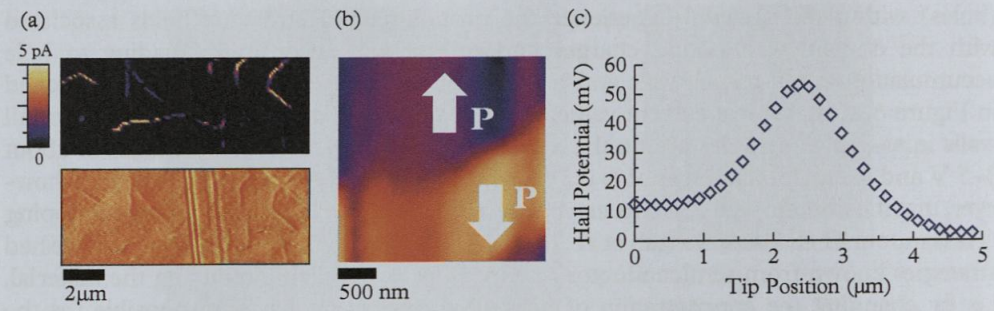

Figure 6.3 *(a) Current-carrying tail-to-tail domain walls in $YbMnO_3$ (top panel) show a distinct Hall voltage signal (bottom panel). Quantitative KPFM was used across the $ErMnO_3$ tail-to-tail domain wall shown in (b) to generate the Hall voltage peak seen in (c).*

Source: (a) is slightly modified from Campbell et al. 2016. (b,c) are slightly adapted from Turner et al. 2018.

second, that the number density of carriers active in transport (and contributing to the Hall effect) is much smaller than that needed to screen the bound charge associated with the polar discontinuity (between three and seven orders of magnitude smaller). This clearly suggests that either the walls are not fully screened, or that an extremely small subset of screening charges is active in conduction; third, that the carrier mobilities are surprisingly high (on the order of 100 $cm^2V^{-1}s^{-1}$ at room temperature). Such mobilities are noteworthy, as they are among the highest reported in oxide systems to date. Dimensional confinement in 2D systems does often seem to be associated with elevated carrier mobility (in graphene and in lanthanum aluminate–strontium titanate interfaces, for example), but these observations in $YbMnO_3$ and $ErMnO_3$ demand confirmation and an extension of research to specifically examine carrier mobilities at low temperature.

In 2017, Mundy et al. (2017) demonstrated that charged head-to-head domain walls in $ErMnO_3$ could also deliver enhanced conduction over bulk, but only under significant electric fields. Turner and co-workers have very recently measured the Hall voltages associated with these conducting head-to-head walls. It is clear that, in these walls, the active carriers are n-type. This presents extremely interesting possibilities for domain wall electronics in the hexagonal manganites, as both p and n-type walls can be simultaneously active in carrying current. Moreover, the microstructure characteristic of the manganites is such that domain walls meet regularly at sixfold vertices, potentially creating arrays of 1D p-n junctions. There is a genuine opportunity to exploit such p-n junctions to allow domain walls to not only act as current carriers for mobile interconnects, but to also become active electronic devices in their own right.

6.2.3 Emulation of Electronic Components

In proper ferroelectrics, such as $BiFeO_3$, $LiNbO_3$, and $BaTiO_3$, conducting domain walls are very mobile and can readily be created, moved, and erased at moderate bias voltages (Seidel et al. 2009; Whyte et al. 2014). This degree of flexibility has

triggered the idea of using them as active elements and control resistivity by writing and erasing conducting domain walls, realizing multi-configurational devices and non-volatile domain wall memory (Jiang et al. 2017; Sharma et al. 2017). In contrast to the easy-to-write/easy-to-erase type of domain walls in $BiFeO_3$, $LiNbO_3$, and $BaTiO_3$, the walls in hexagonal manganites stand out because of their extraordinary stability (Hassanpour et al. 2016; Schoenherr et al. 2019). Analogous to proper ferroelectric domain walls, it is possible to control the density of domain walls (Griffin et al. 2012; Lin et al. 2014; Meier et al. 2017) and set their position by electric-field poling (Han et al. 2013; Chen et al. 2016; Ruff et al. 2018). However, the domain wall density is adjusted at a high temperature ($\gtrsim$1000 K) and to induce domain wall movements, high electric fields, ca. 100 kV/cm at 120 K, are required (Ruff et al. 2018). Thus, within the temperate and voltage regimes relevant for applications in the field of nanoelectronics, the improper ferroelectric domain walls in $RMnO_3$ represent stable, stationary 2D objects. This stability opens up conceptually new opportunities for domain-wall-based applications—instead of using the walls as rewritable wires in classical two- or three-terminal device architectures, the wall itself becomes the device.

A first proof-of-concept study by Mundy et al. (2017) showed that domain wall currents can be gated by application of an electrical voltage, emulating the behavior of a digital switch as presented in Figure 6.4(a,b). While head-to-head domain walls in $RMnO_3$ are insulating with respect to the surrounding bulk at low voltage (Figure 6.2(b)), enhanced conductance is observed at higher voltages ($\gtrsim$5 V, inset to Figure 6.4(a)). This behavior can be explained by the formation of an electric inversion layer at the head-to-head walls as sketched in Figure 6.4(a). Because of the positive domain wall bound charges, the valence-band maximum (VBM) shifts downwards at the head-to-head walls, generating the aforementioned hole depletion region—see inset to Figure 6.4(a). In addition, strong band bending can cause the conduction-band

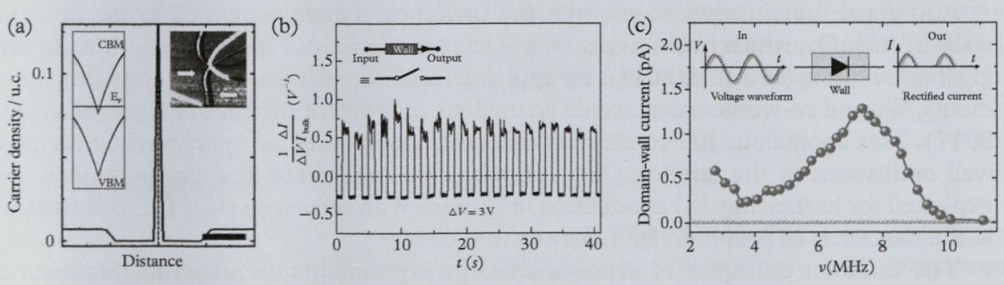

Figure 6.4 *Domain walls as functional circuit elements. (a) Calculated band bending at a head-to-head domain wall, inset is cAFM image showing local inversion layer at head-to-head domain wall—light colors represent higher conductivity. (b) Normalized current at a domain wall as a function of time, demonstrating how domain walls can be used as functional elements: in this case, as switches. (c) The frequency-dependent response of a single neutral domain wall in hexagonal $ErMnO_3$, with insets illustrating the diode-like properties of the wall.*

Source: (a) and (b) are slightly modified from original work by Mundy et al. (2017). (c) is slightly modified from original work by Schaab et al. (2018).

minimum to dip below the Fermi energy, resulting in the representative carrier density distribution shown in Figure 6.4(a). The realization of this carrier distribution in $R\mathrm{MnO_3}$ single crystals is corroborated by the cAFM scan taken at 9 V in the inset to Figure 6.4(a), showing enhanced conductance right at the wall (bright), framed by a region with conductance lower than the surrounding bulk (dark). The observation of insulating head-to-head walls at low voltages can thus be understood in terms of hole depletion, which overrides the emergent electron accumulation. In contrast, at higher voltages, electrons dominate the domain wall transport, giving rise to enhanced conductance relative to the bulk. This effect allows reversible switching between resistive and conductive behavior by applying a variable gate voltage, emulating the functionality of a binary switch as shown in Figure 6.4(b).

A second example of the functionality of improper ferroelectric domain walls in $R\mathrm{MnO_3}$ is the diode-like behavior that arises when a conducting wall is brought in contact with a metallic probe tip. By applying AC voltages with frequencies in the kilo- to megahertz range, i.e. frequencies for which the domain walls are effectively pinned, Schaab and co-workers observed electrical half-wave rectification at the tip–wall contact when measuring the DC output signal (Schaab et al. 2018). The diode-like response is presented in Figure 6.4(c), showing the measured domain wall current (DC) as function of the frequency of the applied AC voltage. The data indicates rectifying domain wall properties for frequencies $\lesssim$10 MHz for a voltage amplitude of 3 V. The effect was explained based on the distinct Schottky barrier forming at the tip–wall interface, which is higher at the domain wall than in the surrounding bulk whenever $\sigma_{\mathrm{wall}} > \sigma_{\mathrm{bulk}}$ is fulfilled. Thus, although half-wave rectification has been reported for neutral domain walls, it is independent of the underlying microscopic mechanism and, hence can be expected to generally occur at all domain walls that exhibit enhanced conductivity with respect to the bulk. With this, it becomes possible to use domain walls for alternating-to-direct (AC-to-DC) current conversion, facilitating the design of nanodiodes.

Additional functionality arises from the structural dynamics related to the domain walls in $R\mathrm{MnO_3}$, which begin to play a role at even higher AC frequencies—toward the gigahertz regime (Wu et al. 2017). By applying local impedance spectroscopy measurements, Wu and co-workers discovered anomalous microwave AC conductivity (Wu et al. 2017). This anomalous AC conductivity was explained based on synchronized domain wall oscillations in the terahertz frequency regime—an effect that can potentially be exploited for harnessing AC conduction in systems with otherwise poor DC conduction at the nanoscale as proposed by Tselev et al. (2016).

The different examples of proof-of-concept experiments discussed in this section highlight the emergence of functionalities beyond just conductance at improper ferroelectric domain walls. Particularly interesting is the general possibility of emulating the behavior of electronic components by exploiting intrinsic domain wall properties. This possibility, together with the extraordinary stability and the small width of the walls (5–10 Å; see Figure 6.1), adds a new dimension to the field of domain wall nanoelectronics, foreshadow a promising pathway toward atomic-scale devices and circuitry.

6.3 Boracites

The history of scientific endeavor and discovery within the boracite mineral group has already been eloquently presented by Hans Schmid in a fascinating and engaging personal perspective article (Schmid 2012). In it, he describes how, on attending an international conference in Grenoble in 1958, he and his colleagues were inspired to think how a single-phase material might simultaneously be ferroelectric and ferromagnetic. Driving back to Geneva after the conference, they imagined a perovskite oxide, in which two opposing apical oxygens, in the characteristic MO_6 perovskite octahedra, might be replaced by halogens (or divalent paramagnetic ions): conceptually, this should generate a double-well potential, which could facilitate geometric cation off-centering and hence the possibility of ferroelectricity. Moreover, if the cations contained within such octahedra had a net magnetic moment, then magnetic ordering might also be expected. Their attempts to synthesize targeted oxyhalide perovskites were, however, unsuccessful and so, to keep their hopes alive, they looked at literature to see what oxyhalide compounds containing mixed-ligand octahedra were already known to exist. One such compound was the naturally occurring mineral boracite ($Mg_3B_7O_{13}Cl$).

It was certainly immediately apparent that boracite was crystallographically polar at room temperature: it was one of the systems in which the Curie brothers had established the phenomenon of piezoelectricity in the nineteenth century (Curie and Curie 1880). Moreover, structure determination had shown that the high-temperature (>538 K) high-symmetry cubic and the room-temperature orthorhombic space groups were both non-centrosymmetric piezoelectric ($F\bar{4}3c$ and $Pca2_1$, respectively). Ferroelectricity seemed plausible: other nineteenth-century works (Mack 1884) described how sulfur and lead oxide powders were attracted to the surfaces of heat-cycled boracite crystals in unusual patterns, which hinted at both the existence of domains and, importantly from the perspective of this book, charged domain walls. Direct evidence through hysteretic P-E loop measurement was, however, not easily obtained. Nevertheless, Schmid and co-workers went on to synthesize and characterize a number of different oxyhalide boracites, eventually discovering the first known ferromagnetic-ferroelectric single crystal material ($Ni_3B_7O_{13}I$) (Ascher et al. 1966).

6.3.1 Improper Ferroelectricity in Boracites

Subsequent research (often in which Schmid maintained a leading role) has shown that the boracites are, in fact, improper ferroelectrics. The primary order parameter associated with the paraelectric cubic ($F\bar{4}3c$) to ferroelectric orthorhombic ($Pca2_1$) transition is still seemingly not completely understood (Meyer et al. 1982; Pascual et al. 2009; Feng et al. 2018). This phase transition is accompanied by a modest uniaxial shearing of the high-temperature cubic unit cell and a slight internal redistribution of atoms, such that a net electrical dipole of order ~1 μCcm^{-2} is developed, which lies parallel to the original cubic <100> shear axis. In most cases, the magnitude of the spontaneous polarization scales with the shear angle of the unit cell, but it must be said that these angles are rather small. Indeed, some early reports on the structural

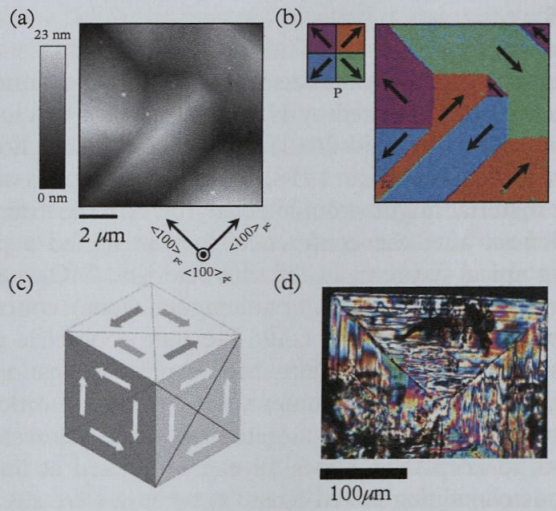

Figure 6.5 *The spontaneous shear associated with the onset of ferroelectricity in boracites is modest (order 0.1°); nevertheless, topographic surface corrugations, induced by different domain variants, are clearly seen using atomic force microscopy (AFM) (a). Such corrugations clearly map onto the different polar orientations revealed by piezoresponse force microscopy (PFM) (b). 90° domain walls show polar discontinuities, suspected as commonplace in naturally occurring Mg-Cl boracite crystals by Schmid (c). Transmission optical microscopy of naturally formed Mg-Cl boracite (d) explicitly shows the quadrant structures illustrated schematically in (c), but also shows that the internal domain microstructure within each quadrant is more complex than given in the schematic.*

Source: (a) and (b) are taken from McQuaid et al. 2017. (c) is loosely adapted from Schmid 2012. (d) is previously unpublished data.

characterization of boracites (Dowty and Clark 1972, 1973; Ito et al. 1951) gave unit cell parameters from diffraction experiments that do not resolve the shear at all. Atomic force microscopy can, however, readily map the surface corrugations that form when a pristine polished crystal is heated and cooled through the ferroelectric phase transition: shear angles at the 0.1° level are easily seen (see Figure 6.5(a)).

There are six equivalent ways in which symmetry can be broken, each generating a different shear strain variant with only one specific direction in polarization. Hence, only six possible polar domain states can form as a result of the symmetry breaking (Dvořák and Petzelt 1971; Erhart 2004; Hlinka et al. 2016), and these can, in principle, be directly mapped using PFM, as can be seen in Figure 6.5(b). However, few aspects of boracite behavior are straightforward to understand, and PFM domain mapping is no exception: in all other known ferroelectrics examined to date, the electric-field-induced movement of the tip–sample contact point lies parallel to the polarization axis. In boracites (or at least in the $Cu_3B_7O_{13}Cl$ crystals studied recently (McQuaid et al. 2017)), conventional vector PFM generates polar directions at 90° to those allowed by symmetry, and hence data must be interpreted differently to give physically meaningful insight. Dvořák (1972) has

suggested that the electromechanical coupling equations in improper ferroelectrics may differ from their usual form in proper ferroelectrics, and this may provide the platform upon which unusual PFM behavior might be fully rationalized.

As well as accounting for the domain states, symmetry considerations also dictate the nature and crystallographic orientation of the domain *walls* that can form in the boracites: {100}pseudocubic (pc) oriented walls delineate ferroelastic shear variants that have 180° anti-aligned polarization's on either side. These 180° walls are fully elastically compatible; moreover, the polarization axes, in the domains themselves, lie parallel to the walls, and hence the walls are uncharged. By contrast, group theory analysis and 0-lattice theory (Zimmermann et al. 1970; Erhart 2004) show that although $\{110\}_{pc}$ 90° walls are elastically and structurally viable, they are necessarily charged. In other words, all 90° domain walls show either head-to-head or tail-to-tail polar discontinuities. Although there is undoubtedly an electrostatic energy cost associated with the existence of such walls, they are surprisingly common in naturally formed crystals and have been deemed to be responsible for the microstructural quadrant patterns seen rather ubiquitously in naturally occurring boracite (Figure 6.5(c,d)). In synthetic crystals, according to Schmid [private communication], these charged walls are not seen as often. However, they can be introduced (injected) using point pressure as will be discussed below.

6.3.2 Injection and Motion of Conducting Domain Walls

As in the manganites, polar discontinuities across domain walls in boracites lead to the formation of sheets of bound charges. Near fields produced by these charges may distort the fundamental band structure of the material locally, such that conductivity either increases or decreases due to changes in the energies of intrinsic electronic states; equally, they may cause the aggregation of mobile charged defects that had otherwise been homogeneously distributed throughout the material. In either case, mobile carrier densities are expected to be affected at the charged domain walls, resulting in conductivities that are different from those of the domains themselves. This is verified in $Cu_3B_7O_{13}Cl$ by AFM observations (Figure 6.6a). Notwithstanding issues surrounding the use of PFM to identify polar directions in the Cu-Cl boracites, it seems that tail-to-tail 90° domain walls possess enhanced conductivity, while head-to-head walls show diminished conductivity, compared to bulk.

On cooling through the Curie temperature (~363 K in the case of $Cu_3B_7O_{13}Cl$), charged 90° domain walls do form spontaneously, but not often as extended microstructural features. However, applying point pressure when the crystal is held just below the Curie temperature (pressing with a needle or a pair of tweezers to generate up to 1 GPa locally) causes local deformation and the creation of quadrant features (Figure 6.6(b)). These are extremely similar to those seen in naturally formed Mg-Cl boracite single crystals (Figure 6.5(c,d)), with boundaries parallel to the crystallographic $\{110\}_{pc}$ planes. Although the details of the domain structures are more complex than in the schematic given by Schmid (Figure 6.5(c)), scanning probe microscopy on the Cu-Cl boracites shows that these quadrant boundaries are indeed charged 90° domain walls with enhanced or diminished conductivities. Often, however, these quadrant boundaries

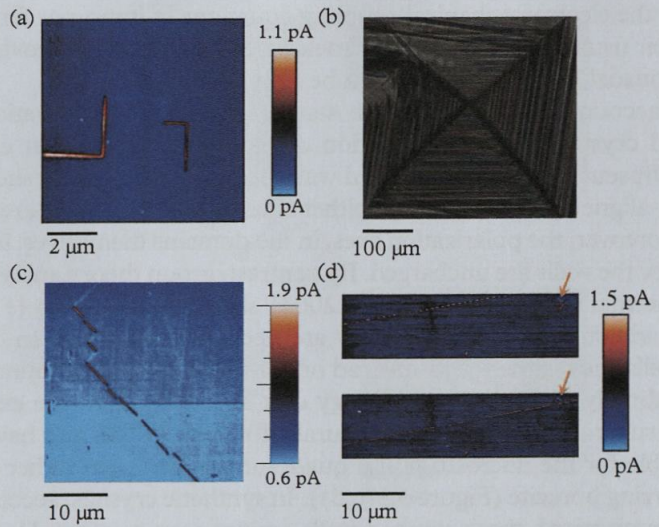

Figure 6.6 *Charged 90° domain walls in $Cu_3B_7O_{13}Cl$ demonstrate different conduction behavior from the domains themselves (a) as revealed through conductive atomic force microscopy (cAFM), revealing tail-to-tail domain walls with enhanced conductance (bright) and head-to cAFM. Point pressure applied just below the Curie temperature can induce domain restructuring into quadrants reminiscent of those formed in naturally occurring $Mg_3B_7O_{13}Cl$ crystals, revealed here (b) by optical microscopy. Quadrant boundaries are composed of charged 90° domain walls, but they can be mixed in nature and hence create discontinuous conduction pathways (c). Importantly, motion does not change the conducting nature of the walls (d), as can be seen in the cAFM maps before and after a wall has been displaced using an electric field. The orange arrows point to the signal from a topographic feature that allows the displacement of the wall between top and bottom panels to be appreciated.*
Source: Panels (a), (b), and (d) reproduced from McQuaid et al. 2017; panel (c) is previously unpublished.

are not entirely head-to-head or tail-to-tail, but instead contain sections of walls with opposite senses of polar discontinuity, and this is reflected in the conducting AFM information (Figure 6.6(c)).

With practice, pressing and dragging point probes can create rather long unbroken sections of 90° domain walls, up to hundreds of microns in length. Controlled motion of these unbroken walls is exciting, from the point of view of domain wall electronics, and it is noteworthy that they can be moved using applied electric fields and that the conductivity of the wall is preserved (Fig. 6.6(d)) (McQuaid et al. 2017). It seems that the planes of enhanced conductivity cannot be easily dissociated from the domain walls themselves, as has been the case in $BiFeO_3$, for example (Stolichnov et al. 2014). This possibly points toward a more intrinsic origin for the domain wall conductivity seen in the boracites. Very recent explorations suggest that the sense in which 90° domain walls move under applied electric fields can be unique, and work is ongoing to rationalize this unexpected behavior.

6.4 Spin-Driven Improper Ferroelectrics

6.4.1 Fundamentals

Magnetic order can break spatial inversion symmetry and thereby drive the emergence of a spontaneous electric polarization. This effect was first reported by Newnham et al. (1978) for Cr_2BeO_4 in 1978 and rationalized by Bar'yachtar et al. (1983) and Bar'yakhtar et al. (1985) in analogy with the flexoelectric effect in liquid crystals. Later on, this phenomenon attracted worldwide attention after Kimura et al. observed pronounced magnetoelectric couplings between spin-spiral order and magnetically induced improper ferroelectricity in $TbMnO_3$ in 2003 (Kimura et al. 2003). In the following years, a wide range of materials was demonstrated to exhibit spin-driven ferroelectric order, and different mechanisms were established as reviewed, for example, in Kimura (2007), Picozzi and Stroppa (2012), Tokura et al. (2014), and Bousquet and Cano (2016). Here, we will focus on the so-called *inverse* Dzyaloshinskii–Moriya (DM) interaction (Katsura et al. 2005; Mostovoy 2006; Sergienko and Dagotto 2006), which is relevant for the domain wall phenomena discussed in Section 6.4.2.

In non-centrosymmetric materials, the magnetic exchange interaction can contain an antisymmetric contribution due to spin–orbit coupling; the DM interaction. The respective energy contribution between neighboring spins $\boldsymbol{S}$ at positions i,j can be written as $E_{DM} \sim \sum_{ij} \boldsymbol{D}_{ij} (\boldsymbol{S}_i \times \boldsymbol{S}_j)$, where $\boldsymbol{D}_{ij}$ is the DM vector $(\boldsymbol{D}_{ij} = -\boldsymbol{D}_{ji})$. Unlike simple symmetric exchange interactions $(\sim \boldsymbol{S}_i \cdot \boldsymbol{S}_j)$, the DM interaction favors a noncollinear arrangement of the spins, and hence can lead to helicoidal, conical, and cycloidal spin structures as illustrated in Figure 6.7(a). Magnetically induced ferroelectricity can be obtained due to the inverse effect. That is, if the spontaneous order of spins lacks inversion symmetry by itself, it can further induce a polar displacement as a secondary order parameter. A simple formula describing the relation between the ordered spins and the induced ferroelectric polarization via the inverse DM effect was derived by Mostovoy (2006), $\boldsymbol{P} \sim \boldsymbol{e}_{ij} \times (\boldsymbol{S}_i \times \boldsymbol{S}_j)$, indicating a one-to-one correlation between the vector chirality $(\boldsymbol{C} = \boldsymbol{S}_i \times \boldsymbol{S}_j)$ of the spin structure and the orientation of P ($\boldsymbol{e}_{ij}$ is the unit vector between neighboring spins). This is illustrated in the lower part of Figure 6.7(a), showing that spin cycloids of opposite chirality induce opposite polar displacements ($+\boldsymbol{C} \leftrightarrow +\boldsymbol{P}$ and $-\boldsymbol{C} \leftrightarrow -\boldsymbol{P}$).

Because of the rigid correlation between magnetism and ferroelectricity, magnetically induced ferroelectrics develop intriguing hybrid domains with inseparably entangled magnetic and electric order parameters, which was first demonstrated in nonlinear optical microscopy measurements $MnWO_4$ (Meier et al. 2009a, 2009b). On the bulk level, such correlations are now well understood, and readers looking for a comprehensive coverage of spin-driven ferroelectricity are referred to more extensive reviews and books on microscopic mechanisms in multiferroics (Kimura 2007; Tokura et al. 2014; Fiebig et al. 2016; Stojanovic 2018). Most importantly for this chapter, recent investigations at the local scale highlight the promising potential of the strong magnetoelectric correlations in spin-driven improper ferroelectrics for the field of domain wall nanoelectronics, as we will discuss in the next section.

6.4.2 Configurational Domain Wall Control with Magnetic Fields and Light

Among the spin-driven improper ferroelectrics, $Mn_{0.95}Co_{0.05}WO_4$ is outstanding because its polarization $\boldsymbol{P}$ gradually rotates by about 90° (i.e. from the crystallographic *b*- to the *a*-axis) under application of a magnetic field (Leo et al. 2015). This effect is remarkably different from other spin-spiral systems, such as $TbMnO_3$, $DyMnO_3$, and $MnWO_4$, where magnetic fields induce a first-order flop of $\boldsymbol{P}$. The continuous polarization rotation in $Mn_{0.95}Co_{0.05}WO_4$ gives the opportunity to gradually modify the configuration of domain wall bound charges as summarized in Figure 6.7(b,c). Figure 6.7(b) shows the magnetic/electric hybrid domains in $Mn_{0.95}Co_{0.05}WO_4$ at 5 K after zero-field cooling ($T_C = 12$ K). The optical second harmonic (SHG) image reflects the position of 180° domain walls by dark lines, across which both $\boldsymbol{C}$ and $\boldsymbol{P}$ reverse sign as explained in Manz et al. (2016). The image reveals that—analogous to the cases of $RMnO_3$ (Section 6.2) and $Cu_3B_7O_{13}Cl$ (Section 6.3)—domain wall sections with head-to-head and tail-to-tail configuration naturally arise in $Mn_{0.95}Co_{0.05}WO_4$. The presence of these walls reflects that the electric dipole–dipole interactions, which usually make such walls energetically unfavorable, are overruled by the energy gain associated with the underlying primary magnetic order parameter.

In spite of the secondary nature of the ferroelectric order, however, Leo et al. (2015) demonstrated that the domain walls in $Mn_{0.95}Co_{0.05}WO_4$ can be controlled by an electrical field. After preparing a sample into a single domain state, they managed to inject and position a side-by-side domain wall by application of an electric field, which remained stationary after removing the field. By application of a magnetic field, the team then gradually rotated the polarization, turning the side-by-side domain wall into a nominally charged wall as presented in Figure 6.7(c). This magnetoelectric manipulation shows the general possibility of controlling the electronic domain wall configuration in a deterministic and reversible process. The emergence of domain wall bound charges at domain walls $Mn_{0.95}Co_{0.05}WO_4$ suggested by the nonlinear optical data was corroborated by atomistic Landau–Lifshitz–Gilbert (LLG) simulations. The LLG simulations revealed that side-by-side domain walls as in Figure 6.7(c) (upper panels) are not simple Ising walls but have a finite Néel component, which is preserved for the induced head-to-head wall (Figure 6.7(c), lower panels). Because of the genuine Néel component that gives $\partial_a P_a = -\rho_{bound} < 0$ across the wall, these domain walls can be expected to get charged with a density of bound charges up to 10^5 C m^{-3}.

Performing similar measurements on the $TbMnO_3$, Matsubara et al. (2015b) showed that conversion of domain wall charge states is a rather general effect in spin-driven improper ferroelectrics and is not restricted to the case of continuous polarization rotations. Although the magnetically driven reorientation of the electric polarization in $TbMnO_3$ occurs through a first-order phase transition, the domain walls can be reversibly tuned between side-by-side and head-to-head/tail-to-tail configurations, pegged to their location by the magnetic order. Going beyond domain wall manipulation via electric and magnetic fields, it was demonstrated that the hybrid domain walls in spin-driven improper ferroelectrics can be controlled optically. By scanning a laser

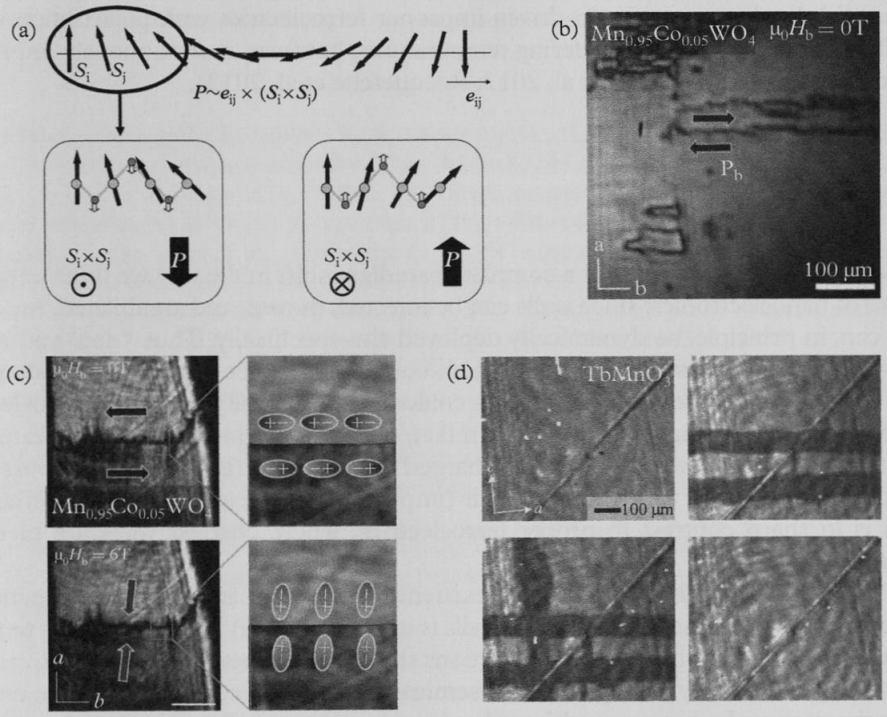

Figure 6.7 *SHG of spin driven multiferroics. (a) Schematic illustration of a spin cycloid. The spin structure violates inversion symmetry and, as a consequence, induces a spontaneous polarization* $\boldsymbol{P}$ *as explained in the main text. The chirality of the cycloid* $\left(C = \boldsymbol{S}_i \times \boldsymbol{S}_j\right)$ *determines the direction of* $\boldsymbol{P}$ *as illustrated in the lower part. Larger arrows represent localized spins* $\boldsymbol{S}$ *(e.g., at Mn sites), and smaller arrows show the spin-driven displacement of intermediary ions (e.g., O). (b) SHG image of ferroelectric domain structure at 5.5 K after cooling in zero field. The dark lines are the ferroelectric domain walls. (c) SHG image of the ferroelectric domain structure at a single wall under 0 T (top) and 6 T (bottom). The magnetic field is used to rotate the polarization direction so that neutral walls (top) have a charge discontinuity in the ferroelectric polarization. (d) SHG image of the ferroelectric domain structure in* $TbMnO_3$ *showing how ferroelectric domains can be written and erased with optical pulses.*

Source: (b) and (c) are slightly modified from original work by Leo et al. (2015). (d) is taken from Manz et al. 2016.

(continuous wave or pulsed) and adjusting the wave length, Manz et al. (2016) wrote and erased side-by-side and head-to-head/tail-to-tail walls in $TbMnO_3$, highlighting the possibility of optical domain wall engineering and patterning (Figure 6.7(d)).

The low value of the electric polarization and the cryogenic temperature at which current model systems, such as $Mn_{0.95}Co_{0.05}WO_4$ and $TbMnO_3$, exhibit hybrid magnetic/electric domain walls undermine the technological advantages. The expected domain wall conductance in $Mn_{0.95}Co_{0.05}WO_4$, for example, is on the order of a few femtoamperes, which is challenging to detect even under laboratory conditions. The

successful development of spin-driven improper ferroelectrics with polarization values $> 1000\ \mu C\ m^{-2}$ and higher ordering temperatures, however, is continuously improving these odds (see, e.g. Johnson et al. 2012; Rocquefelte et al. 2013).

6.5 Outlook

Conducting domain walls offer a complete paradigm shift in the way we think about the future of nanoelectronics: since walls can be injected, moved, and annihilated, functionality can, in principle, be dynamically deployed site-specifically. Thus "now-you-see-it-now-you-don't" ephemeral circuitry, which could exist in one form in one instant and then be completely reconfigured the next, could become a reality. Improper ferroelectrics are particularly exciting in this respect. In fact, one of their most outstanding features is that they naturally provide conducting, charged domain walls (those which support polar discontinuities) by the very nature of their (improper) spontaneous electric polarization. This is in sharp contrast to proper ferroelectrics, where charged walls are meta- or unstable.

The discovery of the simultaneous existence of both *n*- and *p*-type conduction in oppositely charged manganite domain walls is unique (to date) and profound in terms of its potential implications: active *p-n* junctions should be formed at domain wall vertices, and this opens the way for a plethora of semiconducting devices built *inside* the domain walls themselves. In one sense, this makes improper ferroelectrics the front-runners in terms of dynamic domain wall nanoelectronics.

However, the truth is that none of the improper systems discussed above is perfect: all are rather complex in their chemistry, and no single material offers the full gamut of complete domain reconfigurability combined with domain wall functionality that is really needed. Thus, there is a great deal of work yet to be done in modifying currently known materials to expand their properties and map new improper systems. This is not all: a great deal of potentially revolutionary domain wall physics has not yet been explored, which could turn out to be both useful and exotic. For example, genuine confinement effects in domain wall conduction properties (quantum Hall, cyclotron resonance, etc.) have not yet been established; large, potentially giant, carrier mobilities need to be verified and explored further as a function of temperature; opportunities and possibilities for spintronics along walls need to be investigated (Rashba effects, for example) and the basic band structures of domain walls as functional materials in their own right need to be mapped. The domain wall is, after all, a new kind of functional material which may be as exciting as any 2D material known to date.

In summary, improper ferroelectrics are a toolbox with extensive possibilities for the design of new nanoelectronics devices; however, challenges remain to be overcome in the choice and processing of these materials. Further studies of domain walls in improper ferroelectrics will lead to the discovery of new properties that may prove practically useful in these exotic two-dimensional systems.

REFERENCES

Artyukhin S., Delaney K. T., Spaldin N. A., Mostovoy M., "Landau theory of topological defects in multiferroic hexagonal manganites," *Nat. Mater.* 13, 42 (2013).

Ascher E., Rieder H., Schmid H., Stössel H., "Some properties of ferromagnetoelectric nickel-iodine boracite, $Ni_3B7O_{13}I$," *J. Appl. Phys.* 37(3), 1404–1405 (1966).

Bar'yachtar V. G., L'vov V. A., Yablonskii D. A., "Theory of inhomogeneous magnetoelectric effect," *Pisma Zh. Eksp. Teor. Fiz.* 37(12), 565–567 (1983).

Bar'yakhtar V. G., Stefanovskii E. P., Yablonskii D. A., "Theory of magnetic structure and electric polarization of the Cr_2BeO_4," *Pisma Zh. Eksp. Teor. Fiz.* 42(6), 258–260 (1985).

Bednyakov P. S., Sluka T., Tagantsev A. K., Damjanovic D., Setter N., "Formation of charged ferroelectric domain walls with controlled periodicity," *Sci. Rep.* 5, 15819 (2015).

Bednyakov P. S., Sturman B. I., Sluka T., Tagantsev A. K., Yudin P. V., "Physics and applications of charged domain walls," *Npj Comput. Mater.* 4(1), 65 (2018).

Bousquet E., Cano A., "Non-collinear magnetism in multiferroic perovskites," *J. Phys.: Condens. Mat.* 28(12), 123001 (2016).

Campbell M. P., McConville J. P. V. V., McQuaid R. G. P. P., Prabhakaran D., Kumar A., Gregg J. M., "Hall effect in charged conducting ferroelectric domain walls," *Nat. Commun.* 7, 13764 (2016).

Cano A., "Hidden order in hexagonal $RMnO_3$ multiferroics (R=Dy -Lu, In, Y, and Sc)," *Phys. Rev. B: Condens. Mat. Mater. Phys.* 89(21), 214107 (2014).

Cano A., Levanyuk, A. P., "Pseudoproper ferroelectricity in thin films," *Phys. Rev. B: Condens. Mat. Mater. Phys.* 81(17), 172105 (2010).

Catalan G., Seidel J., Ramesh R., Scott J., "Domain wall nanoelectronics," *Rev. Mod. Phys.* 84(1), 119–156 (2012).

Chen Z., Wang X., Ringer S. P., Liao X., "Manipulation of nanoscale domain switching using an electron beam with omnidirectional electric field distribution," *Phys. Rev. Lett.* 117(2), 27601 (2016).

Crassous A., Sluka T., Tagantsev A. K., Setter N., "Polarization charge as a reconfigurable quasi-dopant in ferroelectric thin films," *Nat. Nanotechnol.* 10(7), 614–618 (2015).

Curie J., Curie P., "Développement par compression de l'électricité polaire dans les cristaux hémièdres à faces inclinées," *Bull. Minér.* 3, 4, 90–93 (1880).

Dowty E., Clark J. E., "Crystal-structure refinements for orthorhombic boracite, $Mg_7ClB_7O_{13}$, and a trigonal, iron-rich analogue," *Zeitschrift für Kristallographie* 138(1–6), 64–99 (1973). ISSN (Online) 2196-7105, ISSN (Print) 2194-4946. DOI: https://doi.org/10.1524/zkri.1973.138.jg.64

Dowty E., Clark J. R., Atomic displacements in ferroelectric trigonal and orthorhombic boracite structures. *Solid State Commun.* 10(6), 543–548 (1972).

Du Y., Wang X., Chen D., Yu Y., Hao W., Cheng Z., Dou S. X., "Manipulation of domain wall mobility by oxygen vacancy ordering in multiferroic $YMnO_3$," *Phys. Chem. Chem. Phys.* 15(46), 20010–20015 (2013).

Dvořák V., "Boracites—an example of improper ferroelectrics," *Le J. Phys. Colloq.* 33(C2), C2-89–90 (1972).

Dvořák, V., Petzelt, J., "Symmetry aspect of the phase transitions in boracites," *Czech. J. Phys.* 21(11), 1141–1152 (1971).

Eliseev E. A., Morozovska A. N., Svechnikov G. S., Rumyantsev E. L., Shishkin E. I., Shur V. Y., Kalinin S. V., "Screening and retardation effects on 180°-domain wall motion in ferroelectrics: wall velocity and nonlinear dynamics due to polarization-screening charge interactions," *Phys. Rev. B* 78(24), 245409 (2008).

Erhart J., "Domain wall orientations in ferroelastics and ferroelectrics," *Phase Transit.* 77(12), 989–1074 (2004).

Feng J. S., Xu K., Bellaiche L., Xiang H. J., "Designing switchable near room-temperature multiferroics via the discovery of a novel magnetoelectric coupling," *New J. Phys.* 20(5), 53025 (2018).

Fennie C. J., Rabe K. M., "Ferroelectric transition in $YMnO_3$ from first principles," *Phys. Rev. B: Condens. Mat. Mater. Phys.* 72(10), 100103 (2005).

Fiebig M., Lottermoser T., Meier D., Trassin M., "The evolution of multiferroics," *Nat. Rev. Mater.* 1, 16046 (2016).

Fujimura N., Ishida T., Yoshimura T., Ito T., "Epitaxially grown $YMnO_3$ film: new candidate for nonvolatile memory devices," *Appl. Phys. Lett.* 69(7), 1011–1013 (1996).

Griffin S. M., Lilienblum M., Delaney K. T., Kumagai Y., Fiebig M., Spaldin N. A., "Scaling behavior and beyond equilibrium in the hexagonal manganites," *Phys. Rev. X* 2(4), 41022 (2012).

Han M.-G., Zhu Y., Wu L., Aoki T., Volkov V., Wang X., Chae S. C., Oh Y. S., Cheong S.-W., "Ferroelectric switching dynamics of topological vortex domains in a hexagonal manganite," *Adv. Mater.* 25(17), 2415–2421 (2013).

Hassanpour E., Wegmayr V., Schaab J., Yan Z., Bourret E., Lottermoser Th., Fiebig M., Meier D., "Robustness of magnetic and electric domains against charge carrier doping in multiferroic hexagonal $ErMnO_3$," *New J. Phys.* 18(4), 43015 (2016).

Hlinka J., Privratska J., Ondrejkovic P., Janovec V., "Symmetry guide to ferroaxial transitions," *Phys. Rev. Lett.* 116(17), 177602 (2016).

Holstad T. S., Evans D. M., Ruff A., Småbråten D. R., Schaab J., Tzschaschel Ch., Yan Z., Bourret E., Selbach S. M., Krohns S., Meier D., "Electronic bulk and domain wall properties in B-site doped hexagonal $ErMnO_3$," *Phys. Rev. B* 97(8), 85143 (2018).

Holtz M. E., Shapovalov K., Mundy J. A., Chang C. S., Yan Z., Bourret E., Muller D. A., Meier D., Cano A., "Topological defects in hexagonal manganites: inner structure and emergent electrostatics," *Nano Lett.* 17(10), 5883–5890 (2017).

Huang F.-T., Cheong S.-W., "Aperiodic topological order in the domain configurations of functional materials," *Nat. Rev. Mater.* 2(3), 17004 (2017).

Ito T., Morimoto N., Sadanaga R., "The crystal structure of boracite," *Acta Crystall.* 4(4), 310–316 (1951).

Jiang J., Bai Z. L., Chen Z. H., He L., Zhang D. W., Zhang Q. H., Shi J. A., Park M. H., Scott J. F., Hwang C. S., Jiang A. Q., "Temporary formation of highly conducting domain walls for non-destructive read-out of ferroelectric domain-wall resistance switching memories," *Nat. Mater.* 17, 49 (2017).

Johnson R. D., Chapon L. C., Khalyavin D. D., Manuel P., Radaelli P. G., Martin, C., "Giant improper ferroelectricity in the ferroaxial magnet $CaMn_7O_{12}$," *Phys. Rev. Lett.* 108(6), 67201 (2012).

Katsura H., Nagaosa N., Balatsky A. V., "Spin current and magnetoelectric effect in noncollinear magnets," *Phys. Rev. Lett.* 95(5), 57205 (2005).

Keve E. T., Abrahams S. C., Bernstein J. L., "Ferroelectric ferroelastic paramagnetic beta-$Gd_2(MoO_4)_3$ crystal structure of the transition-metal molybdates and tungstates. VI," *J. Chem. Phys.* 54(7), 3185–3194 (1971).

Kimura, T., "Spiral magnets as magnetoelectrics," *Annu. Rev. Mater. Res.* 37(1), 387–413 (2007).

Kimura T., Goto T., Shintani H., Ishizaka K., Arima T., Tokura Y., "Magnetic control of ferroelectric polarization," *Nature* 426(6962), 55–58 (2003).

Leo N., Bergman A., Cano A., Poudel N., Lorenz B., Fiebig M., Meier D., "Polarization control at spin-driven ferroelectric domain walls," *Nat. Commun.* 6, 4–9 (2015).

Levanyuk A. P., Sannikov D. G., "Improper ferroelectrics," *Soviet Phys. Uspekhi* 17(2), 199–214 (1974).

Lilienblum M., Lottermoser T., Manz S., Selbach S. M., Cano A., Fiebig M., "Ferroelectricity in the multiferroic hexagonal manganites," *Nat. Phys.* 11, 1070 (2015).

Lin S.-Z., Wang X., Kamiya Y., Chern G.-W., Fan F., Fan D., Casas B., Liu Y., Kiryukhin V., Zurek W. H., Batista C. D., Cheong S.-W., "Topological defects as relics of emergent continuous symmetry and Higgs condensation of disorder in ferroelectrics," *Nat. Phys.* 10, 970 (2014).

Lines M. E., Glass A. M., *Principles and Applications of Ferroelectrics and Related Materials. Oxford Classic Texts in the Physical Sciences* (Oxford University Press, Oxford, 2001). doi:10.1093/acprof:oso/9780198507789.001.0001

Mack K., "Ueber das pyroelektrische Verhalten des Boracits," *Z. Kristallogr.– Crystall. Mater.* 8, 503–522 (1884).

Manz, S., Matsubara M., Lottermoser T., Büchi J., Iyama A., Kimura T., Meier D., Fiebig M., "Reversible optical switching of antiferromagnetism in $TbMnO_3$," *Nat. Photon.* 10(10), 653–656 (2016).

Matsubara M., Manz S., Mochizuki M., Kubacka, T., Iyama A., Aliouane N., Kimura T., Johnson S., Meier D., Fiebig M., "Magnetoelectric domain control in multiferroic $TbMnO_3$," *Science* 348(6239), 1112–1115 (2015a).

Manz S., Matsubara M., Lottermoser T., Büchi J., Iyama A., Kimura T., Meier D., Fiebig M., "Reversible optical switching of antiferromagnetism in $TbMnO_3$," *Nat. Photon.* 10(10), 1112–1115 (2015b).

McQuaid R. G. P., Campbell M. P., Whatmore R. W., Kumar A., Gregg J. M., "Injection and controlled motion of conducting domain walls in improper ferroelectric Cu-Cl boracite," *Nat. Commun.* 8, 15105 (2017).

Meier D., "Functional domain walls in multiferroics," *J. Phys.: Condens. Mat.* 27(46) (2015). doi:10.1088/0953–8984/27/46/463003

Meier D., Leo N., Maringer M., Lottermoser Th., Fiebig M., Becker P., Bohatý L., "Topology and manipulation of multiferroic hybrid domains in $MnWO_4$," *Phys. Rev. B* 80(22), 224420 (2009a).

Meier D., Maringer M., Lottermoser T., Becker P., Bohatý L., Fiebig M., "Observation and coupling of domains in a spin-spiral multiferroic," *Phys. Rev. Lett.* 102(10), 107202 (2009b).

Meier D., Seidel J., Cano A., Seidel J., Cano A., Delaney K., Kumagai Y., Mostovoy M., Spaldin N. A., Ramesh R., Fiebig M., "Anisotropic conductance at improper ferroelectric domain walls," *Nat. Mater.* 11(4), 284–288 (2012).

Meier Q. N., Lilienblum M., Griffin S. M., Lilienblum M., Griffin S. M., Conder K., Pomjakushina E., Yan Z., Bourret E., Meier D., Lichtenberg F., Salje E. K. H., Spaldin N. A., Fiebig M., Cano A., "Global formation of topological defects in the multiferroic hexagonal manganites," *Phys. Rev. X* 7(4), 41014 (2017).

Merz W. J., "The electric and optical behavior of $BaTiO_3$ single-domain crystals," *Phys. Rev.* 76(8), 1221–1225 (1949).

Meyer G. M., Nelmes R. J., Thornley F. R., Stirling W. G., "An inelastic neutron-scattering study of the improper ferroelectric transition in copper chlorine boracite," *J. Phys. C: Solid State Phys.* 15(13), 2851–2866 (1982).

Mostovoy M., "Ferroelectricity in spiral magnets," *Phys. Rev. Lett.* 96(6), 67601 (2006).

Mundy J. A., Schaab J., Kumagai Y., Cano A., Stengel M., Krug I. P., Gottlob D. M., Dog Anay H., Holtz M. E., Held R., Yan Z., Bourret E., Schneider C. M., Schlom D. G., Muller D. A., Ramesh R., Spaldin N. A., Meier D., "Functional electronic inversion layers at ferroelectric domain walls," *Nat. Mater.* 16(6), 622 (2017).

Newnham R. E., Kramer J. J., Schulze W. A., Cross L. E., "Magnetoferroelectricity in Cr_2BeO_4," *J. Appl. Phys.* 49(12), 6088–6091 (1978).

Oh Y. S., Luo X., Huang F.-T., Wang Y., Cheong S.-W., "Experimental demonstration of hybrid improper ferroelectricity and the presence of abundant charged walls in $(Ca,Sr)_3Ti_2O_7$ crystals," *Nat. Mater.* 14, 407 (2015).

Pascual J., Íñiguez J., Iliev M. N., Hadjiev V. G., Meen J., "Phonons in the cubic phase of $Co_3B_7O_{13}$ X (X=Cl, Br, and I) boracites," *Phys. Rev. B: Condens. Mat. Mater. Phys.* 79(10), 104115 (2009).

Pawlik A.-S., Kämpfe T., Haußmann A., Woike T., Treske U., Knupfer M., Büchner B., Soergel E., Streubel R., Koitzsch A., Eng L. M., "Polarization driven conductance variations at charged ferroelectric domain walls," *Nanoscale*, 9(30), 10933–10939 (2017).

Picozzi S., Stroppa A., "Advances in ab-initio theory of multiferroics," *Eur. Phys. J. B* 85(7), 240 (2012).

Rocquefelte X., Schwarz K., Blaha P., Kumar S., Van Den Brink J., "Room-temperature spin-spiral multiferroicity in high-pressure cupric oxide," *Nat. Commun.* 4, 2511 (2013).

Ruff A., Li Z., Loidl A., Schaab J., Fiebig M., Cano A., Yan Z., Bourret E., Glaum J., Meier D., Krohns S., "Frequency dependent polarisation switching in h-$ErMnO_3$," *Appl. Phys. Lett.* 112(18), 182908 (2018).

Sando D., Agbelele A., Rahmedov D., Liu J., Rovillain P., Toulouse C., Infante I. C., Pyatakov A. P., Fusil S., Jacquet E., Carrétéro C., Deranlot C., Lisenkov S., Wang D., Le Breton J. M., Cazayous M., Sacuto A., Juraszek J., Zvezdin A. K., Bellaiche L., Dkhil B., Barthélémy A., Bibes M., "Crafting the magnonic and spintronic response of $BiFeO_3$ films by epitaxial strain," *Nat. Mater.* 12(7), 641–646 (2013).

Schaab J., Cano A., Lilienblum M., Yan Z., Bourret E., Ramesh R., Fiebig M., Meier D., "Optimization of electronic domain-wall properties by aliovalent cation substitution," *Adv. Electron. Mater.* 2(1), 1500195 (2016).

Schaab J., Krug I. P., Nickel F., Gottlob D. M., Doğanay H., Cano A., Hentschel M., Yan Z., Bourret E., Schneider C. M., Ramesh R., Meier D., "Imaging and characterization of conducting ferroelectric domain walls by photoemission electron microscopy," *Appl. Phys. Lett.* 104(23), 232904 (2014).

Schaab J., Skjærvø S. H., Krohns S., Dai X., Holtz M. E., Cano A., Lilienblum M., Yan Z., Bourret E., Muller D. A., Fiebig M., Selbach S. M., Meier D., "Electrical half-wave rectification at ferroelectric domain walls," *Nat. Nanotechnol.* 13(11), 1028–1034 (2018).

Schmid H., "The Dice—Stone der Würfelstein: some personal souvenirs around the discovery of the first ferromagnetic ferroelectric," *Ferroelectrics* 427(1), 1–33 (2012).

Schoenherr P., Shapovalov K., Schaab J., Yan Z., Bourret E. D., Hentschel M., Stengel M., Fiebig M., Cano A., Meier D., "Observation of uncompensated bound charges at improper ferroelectric domain walls," *Nano Lett.*, 19(3), 1659–1664 (2019).

Seidel J., Martin L. W., He Q., Zhan Q., Chu Y. -H., Rother A., Hawkridge M. E., Maksymovych P., Yu P., Gajek M., Balke N., Kalinin S. V., Gemming S., Wang F., Catalan G., Scott J. F., Spaldin N. A., Orenstein J., Ramesh R., "Conduction at domain walls in oxide multiferroics," *Nat. Mater.* 8(3), 229–234 (2009).

Sergienko I. A., Dagotto E., "Role of the Dzyaloshinskii-Moriya interaction in multiferroic perovskites," *Phys. Rev. B: Condens. Mat. Mater. Phys.* 73(9), 94434 (2006).

Sharma P., Zhang Q., Sando D., Lei C. H., Liu Y., Li J., Nagarajan V., Seidel J., "Nonvolatile ferroelectric domain wall memory," *Sci. Adv.* 3(6) (2017).

Skjærvø S. H., Wefring E. T., Nesdal S. K., Gaukås N. H., Olsen G. H., Glaum J., Tybell T., Selbach S. M., "Interstitial oxygen as a source of p-type conductivity in hexagonal manganites," *Nat. Commun.* 7, 13745 (2016).

Sluka T., Tagantsev A. K., Bednyakov P., Setter N., "Free-electron gas at charged domain walls in insulating $BaTiO_3$," *Nat. Commun.* 4(May), 1808 (2013).

Smaabraaten D. R., Meier Q. N., Skjærvø S. H., Inzani K., Meier D., Selbach S. M., "Charged domain walls in improper ferroelectric hexagonal manganites and gallates," *Phys. Rev. Mater.* 2(11), 114405 (2018).

Stojanovic B., *Magnetic, Ferroelectric, and Multiferroic Metal Oxides* (G. Korotcenkov, Ed.), 1st edn. (Elsevier, Amsterdam, Netherlands, 2018).

Stolichnov I., Iwanowska M., Colla E., Ziegler B., Gaponenko I., Paruch P., Huijben M., Rijnders G., Setter N., "Persistent conductive footprints of 109° domain walls in bismuth ferrite films," *Appl. Phys. Lett.* 104(13), 132902 (2014).

Strukov B. A., Levanyuk A. P., "General characteristics of structural phase transitions in crystals," *Ferroelectric Phenomena in Crystals* (B. A. Strukov and A. P. Levanyuk, Eds.), pp. 1–29. (Springer Berlin Heidelberg, Berlin, Heidelberg, 1998).

Tagantsev A. K., Cross L. E., Fousek J., *Domains in Ferroic Crystals and Thin Films. Domains in Ferroic Crystals and Thin Films* (Springer-Verlag, New York, 2010). doi:10.1007/978-1-4419-1417-0

Tokura Y., Seki S., Nagaosa N., "Multiferroics of spin origin," *Rep. Progr. Phys.* 77(7), 76501 (2014).

Tolédano J. C., Tolédano P., *The Landau Theory of Phase Transitions* (World Scientific, Singapore, 1987). doi:10.1142/0215

Tolédano P., "Pseudo-proper ferroelectricity and magnetoelectric effects in $TbMnO_3$," *Phys. Rev. B: Condens. Mat. Mater. Phys.* 79(9), 94416 (2009).

Tolédano P., Mettout B., Schranz W., Krexner G., "Directional magnetoelectric effects in $MnWO_4$: magnetic sources of the electric polarization," *J. Phys.: Condens. Mat.* 22(6), 65901 (2010).

Tselev A., Yu P., Cao Y., Dedon L. R., Martin L. W., Kalinin S. V., Maksymovych P., "Microwave A.C. conductivity of domain walls in ferroelectric thin films," *Nat. Commun.* 7(May), 11630 (2016).

Turner P. W., McConville J. P. V., McCartan S. J., Campbell M. H., Schaab J., McQuaid R. G. P., Amit Kumar J., Gregg J. M., "Large carrier mobilities in $ErMnO_3$ conducting domain walls revealed by quantitative hall-effect measurements," *Nano Lett.* 18(10), 6381–6386 (2018).

Van Aken B. B., Palstra T. T. M., Filippetti A., Spaldin N. A., "The origin of ferroelectricity in magnetoelectric $YMnO_3$," *Nat. Mater.* 3(3), 164–170 (2004).

Wadhawan V., *Introduction to Ferroic Materials* (CRC Press, London, 2000). doi:https://doi.org/10.1201/9781482283051

Whyte J. R., McQuaid R. G. P., Sharma P., Canalias C., Scott J. F., Gruverman A., Gregg J. M., "Ferroelectric domain wall injection," *Adv. Mater.* 26(2), 293–298 (2014).

Wu W., Horibe Y., Lee N., Cheong S.-W., Guest J. R., "Conduction of topologically protected charged ferroelectric domain walls," *Phys. Rev. Lett.* 108(7), 77203 (2012).

Wu X., Petralanda U., Zheng L., Hu R., Cheong S. W., Artyukhin S., Lai K., "Low-energy structural dynamics of ferroelectric domain walls in hexagonal rare-earth manganites," *Sci. Adv.* 3(5) (2017). doi:10.1126/sciadv.1602371

Zimmermann A., Bollmann W., Schmid H., "Observations of ferroelectric domains in boracites," *Phys. Status Solidi (A)* 3(3), 707–720 (1970).